machines

MDPI

Article

Field-Weakening Strategy with Modulated Predictive Current Control Applied to Six-Phase Induction Machines

Magno Ayala [1,*], Jesus Doval-Gandoy [2,*], Jorge Rodas [1], Osvaldo Gonzalez [1], Raúl Gregor [1], Larizza Delorme [1], Carlos Romero [1] and Ariel Fleitas [1]

[1] Laboratory of Power and Control Systems (LSPyC), Facultad de Ingeniería, Universidad Nacional de Asunción, Luque 2060, Paraguay; jrodas@ing.una.py (J.R.); ogonzalez@ing.una.py (O.G.); rgregor@ing.una.py (R.G.); ldelorme@ing.una.py (L.D.); cromero@ing.una.py (C.R.); afleitas@fiuna.edu.py (A.F.)

[2] Applied Power Electronics Technology (APET) Research Group, University of Vigo, 36310 Vigo, Spain

* Correspondence: mayala@ing.una.py (M.A.); jdoval@uvigo.es (J.D.-G.)

Abstract: The predictive current controller has arisen as a practicable technique for operating multiphase machines due to its fast dynamic response, control flexibility, and overall good performance. However, this type of controller has limitations, e.g., it tends to suffer from steady-state tracking errors in $(d-q)$ currents; high computational burden; and high $(x-y)$ currents, which become more pronounced at higher speeds, thereby worsening its sustainability. While some proposals have addressed these limitations by incorporating modulation stages and new cost functions, there is still room for improvement, particularly at higher speeds. In line with the pursuit of sustainable advancements, this article explores the integration of a field-weakening strategy with a modulated predictive current controller applied to a six-phase induction machine to improve its performance at current tracking for higher speed ranges. Experimental tests were conducted to validate the effectiveness of the proposed controller, assessing stator current tracking, reduction in the $(x-y)$ currents, and the total harmonic distortion.

Keywords: field-weakening operation; multiphase induction machine; predictive current control; space vector modulation

Citation: Ayala, M.; Doval-Gandoy, J.; Rodas, J.; Gonzalez, O.; Gregor, R.; Delorme, L.; Romero, C.; Fleitas, A. Field-Weakening Strategy with Modulated Predictive Current Control Applied to Six-Phase Induction Machines. *Machines* **2024**, *12*, 178. https://doi.org/10.3390/machines12030178

Academic Editor: Gyftakis Konstantinos

Received: 30 January 2024
Revised: 22 February 2024
Accepted: 4 March 2024
Published: 6 March 2024

1. Introduction

The scientific and industrial communities have increasingly focused on multiphase machines due to their inherent characteristics, including lower current per phase, fault tolerance, and superior harmonic filtering, compared to their three-phase counterparts [1–3]. Lately, they have gained widespread use in applications such as wind conversion systems, electric vehicles, and general-purpose applications [1,4,5]. The proposed controllers, when applied to multiphase power converters, typically build upon well-established techniques used for three-phase versions. These techniques include field-oriented control (FOC), which involves a proportional-integral (PI) inner control with a modulation stage [6], as well as direct torque control. Direct torque control consists of regulating two variables—stator flux and electrical torque—typically through the use of hysteresis controllers and switching tables that define the stator voltages [7,8]. Recently, there have been exciting advancements in nonlinear control algorithms for multiphase machines. One of these is the sliding mode-based controllers, which have been proposed as a robust and cost-effective alternative to linear controllers [9,10]. However, the discrete control version of model-based predictive control (FCS-MPC) has emerged as one of the most widely used due to its discrete nature and fast transient response compared to other controllers in the literature [11,12]. FCS-MPC offers several other advantages, such as handling multiple objectives and constraints, adapting to different power converters or machine models, and controlling both linear and nonlinear systems. Numerous FCS-MPC variants have been developed in recent years to

address its limitations, such as steady-state tracking error and high computational burden. These variants have shown promising results and can potentially revolutionize the field of multiphase machine control [13–18].

Despite the variety of proposed modifications to overcome the limitations of standard FCS-MPC, little attention has been given to field-weakening (FW) operations. This is surprising considering the practical importance of FW for high-speed operation, particularly in industrial and automotive applications [19]. While traditional methods for achieving maximum torque at high speeds in three-phase machines, such as the stator flux method [20–23], have been extensively studied, this has not been the case for FCS-MPC applied to multiphase machines. Despite stability analyses considering the maximum achievable rotation speed with the controller sampling frequency being performed in some studies, such as [24], the effects of FW on multiphase machines have yet to be thoroughly investigated. As previously reported, induction machines aim to achieve the maximum possible torque at higher speeds than the nominal speed while accounting for electromagnetic FW. To achieve this goal, various methods have been developed for three-phase machines, with the stator flux method being the most widely used, which makes stator flux vary inversely with the motor speed [25]. However, the impact of high-speed operations on FCS-MPC applied to multiphase induction machines is still a largely unexplored area.

For the first time, the operation of electrical drives based on predictive control for multiphase induction machines working in the FW zone is studied. Modifications are presented starting from the previously proposed solutions for three-phase induction motor drives, which allow their integration with the MPCC control in multiphase drives. The theory and experiments in which it is explored are presented. These tests aim to demonstrate the feasibility of using established control techniques such as MPCC with an FW algorithm to enhance the performance of multiphase induction motors for specific applications, such as the automotive industry. They explore new performance and efficiency limits under field-weakening conditions at speeds higher than the nominal, analyzing the motor's behavior regarding the MSE and THD, which are uncommon in predictive control papers. Therefore, this article presents a study and implementation of a modulated FCS-MPC in the high-speed region performed on a six-phase induction machine (SPIM). The controller behavior in high-speed operations conditions is demonstrated through experimental results, which extend the use of modulated FCS-MPC to multiphase induction machines. Note that modulated FCS-MPC, proposed in [16], was chosen as a case study due to its potential for high-speed operations in SPIMs. The results regarding current tracking will be discussed by considering the total harmonic distortion (THD) of stator currents and the mean square error (MSE) of current tracking under the FW operation.

The complete article is presented as follows: In Section II, the SPIM mathematical model is shown. Section III presents the proposed controller, including the FCS-MPC design, which is presented as a predictive current control (PCC), where the traditional PCC is described. Section III also describes the design of the modulated FCS-MPC called MPCC and includes the high-speed operations zone optimization algorithm. The experimental tests present the behavior for the proposed control in transient and steady-state operations. In Section IV, the figures of merit are discussed. Ultimately, the concluding section encapsulates the conclusions and offers final remarks.

2. SPIM State-Space Model

The plant consists of a SPIM powered by a dc power source through a double three-leg voltage source inverter (VSI). In Figure 1, a connection diagram of the system is presented, including the VSI, which is based on IGBT. The SPIM is modeled by differential equations. Then, a vector space decomposition (VSD) method is considered to convert the six-dimensional space of the SPIM with its six phases (a, b, c, d, e, f) into three independent bi-dimensional planes in the stationary reference frame. These new planes are defined as follows: ($\alpha - \beta$), which is related to the electromagnetic energy conversion; ($x - y$) which represents copper losses through positive and negative sequence harmonics; and ($z_1 - z_2$),

which represents the zero sequence harmonics using (1), where an invariant amplitude has been selected [26]. The SPIM exhibits a phase shift of 30° between the three-phase windings and has isolated neutrals, so it is assumed that the currents $(z_1 - z_2)$ are zero.

$$\mathbf{T} = \frac{1}{3}\begin{array}{c} \begin{matrix} a & d & b & e & c & f \\ \downarrow & \downarrow & \downarrow & \downarrow & \downarrow & \downarrow \end{matrix} \\ \begin{bmatrix} 1 & \frac{\sqrt{3}}{2} & -\frac{1}{2} & -\frac{\sqrt{3}}{2} & -\frac{1}{2} & 0 \\ 0 & \frac{1}{2} & \frac{\sqrt{3}}{2} & \frac{1}{2} & -\frac{\sqrt{3}}{2} & -1 \\ 1 & -\frac{\sqrt{3}}{2} & -\frac{1}{2} & \frac{\sqrt{3}}{2} & -\frac{1}{2} & 0 \\ 0 & \frac{1}{2} & -\frac{\sqrt{3}}{2} & \frac{1}{2} & \frac{\sqrt{3}}{2} & -1 \\ 1 & 0 & 1 & 0 & 1 & 0 \\ 0 & 1 & 0 & 1 & 0 & 1 \end{bmatrix} \end{array} \begin{array}{l} \leftarrow \alpha \\ \leftarrow \beta \\ \leftarrow x \\ \leftarrow y \\ \leftarrow z_1 \\ \leftarrow z_2 \end{array} \quad (1)$$

The VSI is discrete and has $2^6 = 64$ possible switching outputs defined as six legs. The dc power source and the switching outputs determine the voltage values per phase and are represented in the $(\alpha - \beta)$ and $(x - y)$ planes according to the VSD method [26]. Figure 2 represents the sixty-four possible values in which only forty-nine different vectors (48 active + 1 null) are different. The SPIM model is presented by:

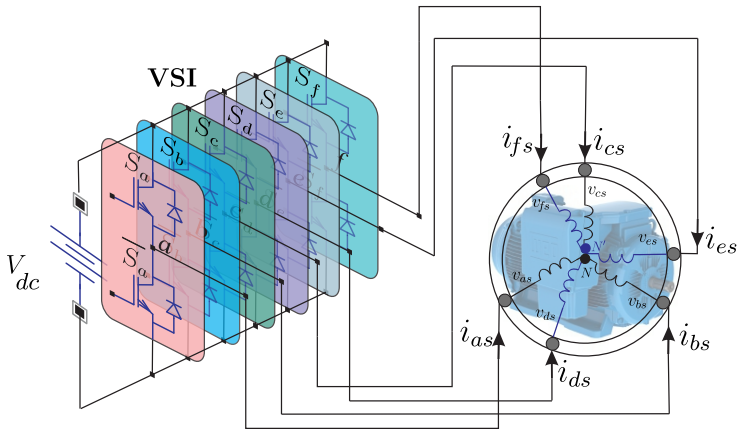

Figure 1. Scheme of SPIM powered by a six-leg VSI.

$$\dot{\mathbf{X}}_{(t)} = \mathbf{A}_{(t)}\,\mathbf{X}_{(t)} + \mathbf{B}_{(t)}\,\mathbf{U}_{(t)} + \mathbf{H}\,\varpi_{(t)} \quad (2)$$

where $\mathbf{X}_{(t)} = [x_1,\, x_2,\, x_3,\, x_4, x_5,\, x_6]^T$ is the state vector that defines the rotor and stator currents $x_1 = i_{\alpha s}$, $x_2 = i_{\beta s}$, $x_3 = i_{xs}$, $x_4 = i_{ys}$, $x_5 = i_{\alpha r}$ and $x_6 = i_{\beta r}$; $\mathbf{U}_{(t)} = [u_1,\, u_2,\, u_3,\, u_4]^T = [v_{\alpha s},\, v_{\beta s},\, v_{xs},\, v_{ys}]^T$ is the input vector applied to the stator coils; $\mathbf{H}$ is considered the disturbance weight matrix; $\varpi_{(t)}$is defined as the process noise; and $\mathbf{A}_{(t)}$ and $\mathbf{B}_{(t)}$ include the physical parameters of the SPIM as shown:

$$\mathbf{A}_{(t)} = \begin{bmatrix} -R_s c_2 & c_4 L_m \omega_r & 0 & 0 & c_4 R_r & c_4 L_r \omega_r \\ c_4 L_m \omega_r & -R_s c_2 & 0 & 0 & c_4 L_r \omega_r & c_4\, R_r \\ 0 & 0 & -R_s c_3 & 0 & 0 & 0 \\ 0 & 0 & 0 & -R_s c_3 & 0 & 0 \\ R_s c_4 & -c_5 L_m \omega_r & 0 & 0 & -c_5 R_r & -c_5\, L_r \\ -c_5 L_m \omega_r & R_s c_4 & 0 & 0 & -c_5 L_r & -c_5\, R_r \end{bmatrix}$$

$$\mathbf{B}_{(t)} = \begin{bmatrix} c_2 & 0 & 0 & 0 \\ 0 & c_2 & 0 & 0 \\ 0 & 0 & c_3 & 0 \\ 0 & 0 & 0 & c_3 \\ -c_4 & 0 & 0 & 0 \\ 0 & -c_4 & 0 & 0 \end{bmatrix}$$

where R_s, R_r, L_m (mutual inductance), $L_s = L_{ls} + L_m$, and $L_r = L_{lr} + L_m$ are the electrical variables of the SPIM. The constants are defined as $c_1 = L_s L_r - L_m^2$, $c_2 = \frac{L_r}{c_1}$, $c_3 = \frac{1}{L_{ls}}$, $c_4 = \frac{L_m}{c_1}$, and $c_5 = \frac{L_s}{c_1}$. The stator voltages are calculated from the input control switching value $\mathbf{S}$. An ideal VSI model $\mathbf{M}_{[\mathbf{S}]}$ was selected to achieve a good optimization calculation. Then, the stator voltages are defined in the following equation [16].

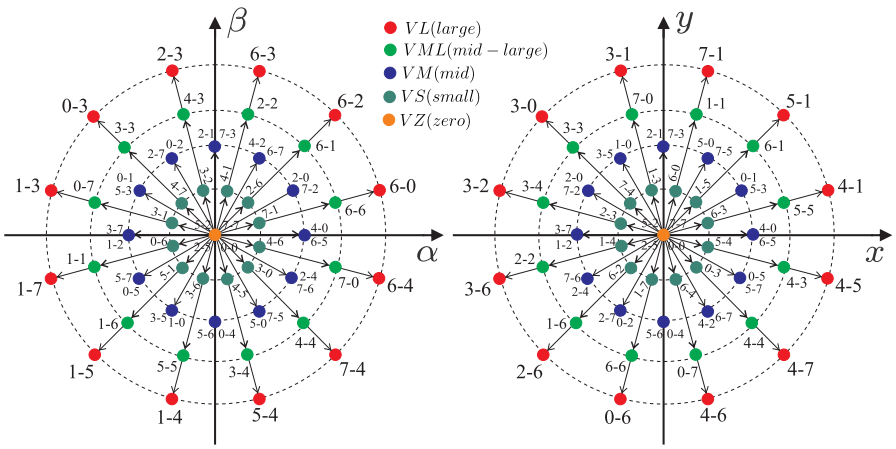

Figure 2. Representation of the 64 voltage vectors for a SPIM in the $(\alpha - \beta)$ and $(x - y)$ planes.

$$\mathbf{M}_{[\mathbf{S}]} = \frac{1}{3}\begin{bmatrix} 2 & 0 & -1 & 0 & -1 & 0 \\ 0 & 2 & 0 & -1 & 0 & -1 \\ -1 & 0 & 2 & 0 & -1 & 0 \\ 0 & -1 & 0 & 2 & 0 & -1 \\ -1 & 0 & -1 & 0 & 2 & 0 \\ 0 & -1 & 0 & -1 & 0 & 2 \end{bmatrix} \mathbf{S}^T. \tag{3}$$

where $\mathbf{S} = [S_a, S_d, S_b, S_e, S_c, S_f]$, $\mathbf{S}_i \in \{0, 1\}$. The VSI generates the phase voltages from the switching values and then converts them into the $(\alpha - \beta)$ and $(x - y)$ planes. Finally, they are defined in $\mathbf{U}_{(t)}$, as follows:

$$\mathbf{U}_{(t)} = V_{dc}\, \mathbf{T}\, \mathbf{M}_{[\mathbf{S}]}. \tag{4}$$

where V_{dc} is the dc power source. $\mathbf{Y}$ is considered the output vector:

$$\mathbf{Y}_{(t)} = \mathbf{C}\, \mathbf{X}_{(t)} + \nu_{(t)} \tag{5}$$

where $\nu_{(t)}$ the measurement noise and

$$\mathbf{C} = \begin{bmatrix} 1 & 0 & 0 & 0 & 0 & 0 \\ 0 & 1 & 0 & 0 & 0 & 0 \\ 0 & 0 & 1 & 0 & 0 & 0 \\ 0 & 0 & 0 & 1 & 0 & 0 \end{bmatrix}.$$

The torque of the SPIM is calculated as follows:

$$T_e = 3\, P\left(\psi_{\alpha s} i_{\beta s} - \psi_{\beta s} i_{\alpha s}\right) \tag{6}$$

$$J_i\, \dot{\omega}_m + B_i\, \omega_m = (T_e - T_L) \tag{7}$$

$$\omega_r = P\omega_m \tag{8}$$

where T_e is the electromagnetic torque, P the number of pole pairs, $\psi_{\alpha s}$ and $\psi_{\beta s}$ are the stator fluxes, J_i is the inertia coefficient, ω_m is the mechanical speed, B_i is the friction coefficient, T_L is the load torque, and ω_r is the rotor electrical angular speed.

3. Proposed Control Applied to the SPIM

This section also presents the complete control structure consisting of outer speed control with an inner PCC; the reduced order observer; the cost function design; the modulated PCC, named MPCC; and the FW operation. Figure 3 displays the control diagram of the entire system.

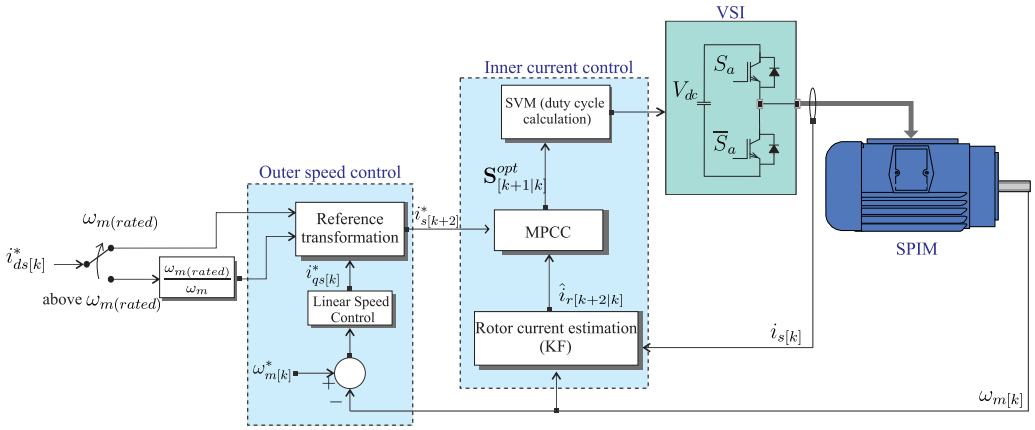

Figure 3. Control diagram including MPCC and the FW operation.

3.1. Rotor Speed Control

The SPIM speed is controlled in this outer loop. A PI controller with a saturator and anti-windup technique, designed in [27], is used for its simplicity and robustness. The PI generates the current reference i^*_{qs}, which is the stator's current reference. Then, the slip frequency (ω_{sl}) calculation is obtained in a similar process as the indirect rotor FOC (IRFOC) through the references of $d-q$ stator currents (i^*_{ds}, i^*_{qs}) and the rotor parameters R_r, L_r of the SPIM. This equation defines the speed control:

$$i^*_{qs} = K_p(\omega^*_m - \omega_m) + \frac{K_i(\omega^*_m - \omega_m)}{s}. \tag{9}$$

3.2. PCC Based on FCS-MPC

SPIMs (2) and (5) have to be in discrete form for the PCC to be able to act. A direct Euler method is performed to keep the computational burden low. These equations are written in digital form, with the variables being predicted using their past values and not the present values. Therefore, the next sample $\hat{\mathbf{X}}_{[k+1|k]}$ is written as follows:

$$\hat{\mathbf{X}}_{[k+1|k]} = \mathbf{X}_{[k]} + \mathrm{f}\Big(\mathbf{X}_{[k]},\, \mathbf{U}_{[k]},\, T_s,\, \omega_{r[k]}\Big) \tag{10}$$

where $[k]$ is the present sample, f is the function nomenclature, and T_s is the sampling time.

3.3. Rotor Current Observers

Only the stator currents and the rotor speed can be measured in the SPIM model (2). The switching values sent to the dual three-phase VSI are used to estimate the stator voltages. On the other hand, the rotor currents cannot be measured, so they have to be estimated. This is achieved through the reduced-order observers. Low-order observers only estimate the unmeasured parts of the state vector. This has been resolved by using the Luenberger Observer (LO) [28], sliding mode control with feedforward [29,30], and Kalman Filter (KF) [31] methods, where the KF is preferable because its gains are calculated by considering the noise measured by the sensors. A deep analysis of the KF is described in [31], and it is not included in this work for brevity.

3.4. Cost Function

This allows for the optimization of essential variables, such as reducing the torque ripple of the machine and minimizing the harmonic content [24]. However, the most crucial variable in current control is the tracking error in stator currents in the $(\alpha - \beta)$ and $(x - y)$ planes. PCC examines the cost function for forty-nine iterations with the following equation:

$$J_{[k+2|k]} = \left[(i^*_{\alpha s[k+2]} - \hat{i}_{\alpha s[k+2|k]})^2 + (i^*_{\beta s[k+2]} - \hat{i}_{\beta s[k+2|k]})^2 + \lambda_{xy} \left((i^*_{xs[k+2]} - \hat{i}_{xs[k+2|k]})^2 + (i^*_{ys[k+2]} - \hat{i}_{ys[k+2|k]})^2 \right) \right]^{\frac{1}{2}} \tag{11}$$

Using (12), it is possible to compute a second step forward prediction of the stator currents $\hat{i}_{s[k+2|k]}$ for the dead time compensation [16]. The stator current references are defined by $i^*_{s[k+2]}$. As for the weighting coefficient, its adjustment is a contemporary research topic, and some papers have addressed this subject [32,33]. Normally, in multiphase machines, λ_{xy} prioritizes the stator currents in the $(\alpha - \beta)$ plane. Applying the square root to the cost function allows the control designer to calculate the duty cycles for each voltage vector within the selected sector considering the geometric distance in the space vector plane.

$$\hat{\mathbf{X}}_{[k+2|k]} = \mathbf{A}_{[k]} \hat{\mathbf{X}}[k+1] + \mathbf{B}_{[k]} \mathbf{U}_{[k+1]} + \mathbf{H} \varpi_{[k]} \tag{12}$$

where $\mathbf{A}_{[k]}$ and $\mathbf{B}_{[k]}$ are discrete versions of the $\mathbf{A}_{(t))}$ and $\mathbf{B}_{(t)}$ matrices, respectively.

3.5. Modulated PCC (MPCC)

MPCC is a technique designed on space vector modulation (SVM). Therefore, MPCC uses four vectors, including two large vectors (LV) and two mid vectors (MV). The objective of this technique is to diminish the stator current error tracking by including the adjacent MV per sector to avoid using null vectors (ZVs). ZVs limit the voltage range of the vectors when combined with the other vectors, increasing the stator current tracking error in the $(\alpha - \beta)$ plane because the ZV duty cycle increases given that the $(x - y)$ currents are trying to be eliminated [16]. The duty cycles, for the four active vectors d_1, d_2, d_3, and d_4 (for example, 4-0, 4-2, 6-0, and 6-2 of Sector I presented in Figure 4), are estimated as follows:

$$d_1 + d_2 + d_3 + d_4 = 1 \tag{13}$$

$$d_1 = \frac{\sigma}{J_1} \quad d_2 = \frac{\sigma}{J_2} \quad d_3 = \frac{\sigma}{J_3} \quad d_4 = \frac{\sigma}{J_4} \tag{14}$$

where J_1, J_2, J_3, and J_4 are the cost function (11) for each vector in the optimal sector that represents the geometric distance from the optimal point to that active vector. It is feasible to define σ and the duty cycles for each vector as follows:

$$d_1 = \frac{J_2 J_3 J_4}{J_1 J_3 J_4 + J_2 J_3 J_4 + J_1 J_2 J_4 + J_1 J_2 J_3} \tag{15}$$

$$d_2 = \frac{J_1 J_3 J_4}{J_1 J_3 J_4 + J_2 J_3 J_4 + J_1 J_2 J_4 + J_1 J_2 J_3} \tag{16}$$

$$d_3 = \frac{J_1 J_2 J_4}{J_1 J_3 J_4 + J_2 J_3 J_4 + J_1 J_2 J_4 + J_1 J_2 J_3} \tag{17}$$

$$d_4 = \frac{J_1 J_2 J_3}{J_1 J_3 J_4 + J_2 J_3 J_4 + J_1 J_2 J_4 + J_1 J_2 J_3} \tag{18}$$

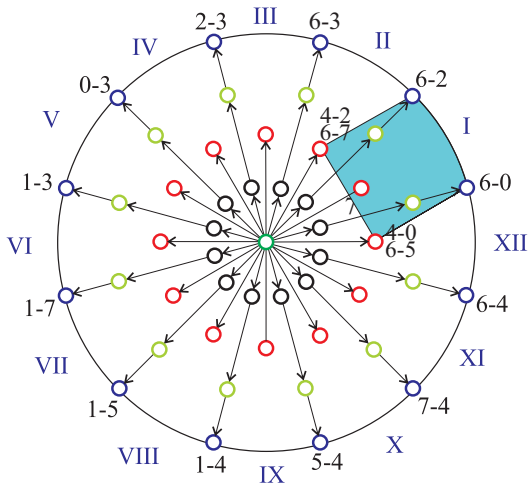

Figure 4. Active 12 sectors of MPCC for the six-leg VSI.

MPCC evaluates 12 sectors (identified by Roman numerals), as depicted in Figure 4, by obtaining the cost function for all the vectors. Then, the duty cycles for each vector are obtained. Next, a final cost function is calculated:

$$G_{[k+2|k]} = d_1 J_1 + d_2 J_2 + d_3 J_3 + d_4 J_4. \tag{19}$$

This last cost function is evaluated in every sampling time for MPCC to select the optimal sector. After that, the duty cycles are calculated with their own cost functions of each vector so that the application of the four vectors generates a control effort that minimizes the stator current tracking error.

3.6. Field-Weakening Operation Applied with MPCC

For FW operations, the simplest method, applied to three-phase machines, is to modify the rotor flux reference in inverse proportion to ω_m [25]. This technique will be examined within this work for the SPIM, which can be adapted directly considering that the IRFOC applied in the $(d-q)$ plane is similar to the three-phase machines. In this technique, when operating above the rated speed, the reference currents i^*_{ds} and i^*_{qs} are computed as follows:

$$i^*_{ds} = \frac{\omega_{m(rated)}}{\omega_m} i_{ds(rated)} \tag{20}$$

$$i^*_{qs(max)} = \sqrt{i^2_{s(max)} - i^{*2}_{ds}} \tag{21}$$

where $i_{s(max)}$ is the maximum possible stator current, normally set to 1.5 times the rated current [20]. At the same time, $i^*_{qs(max)}$ is the maximum possible reference in the case of not having an external speed control; so, in this proposal, it can be used to limit the speed controller output since this value is obtained from the speed control. Usually, when i^*_{ds} is decreased, to use the maximum current, i^*_{qs} can be increased as i^*_{ds} decreases. By combining the above equations, the following is obtained:

$$i^{*2}_{qs(max)} + \left(\frac{\omega_{m(rated)}}{\omega_m} i_{ds(rated)} \right)^2 = i^2_{s(max)}. \tag{22}$$

At the same time, the maximum stator voltage is defined by V_{dc} and modulation synthesizing. Typically, a modulation based on the voltage space vector limits the maximum stator voltage $V_{s(max)}$ to a value of approximately $\frac{V_{dc}}{\sqrt{3}}$ [34]. So, the following equation defines the voltage limits:

$$v^2_{qs} + v^2_{ds} \leq V^2_{s(max)}. \tag{23}$$

In high-speed conditions, the stator resistance effect is low, so the inductance is dominant, as follows [20]:

$$(\omega_r L_s i_{ds})^2 + (\omega_r \frac{L_s L_r - L_m^2}{L_r} i_{qs})^2 \leq V_{s(max)}^2. \tag{24}$$

Under these voltage and current limit conditions, MPCC has to regulate stator currents in the $(\alpha - \beta)$ and $(x - y)$ planes. MPCC can generate larger voltage vectors within the constraints due to the nature of its vector selection. At the same time, the FW zone can be considered two regions separated by a value ω_{FW}, where the first region has a torque reduction behavior due to the inverse of the speed and the second region has a torque reduction behavior due to the inverse of the square of the speed where the slip is constant. This speed, mentioned in [20], can be calculated by:

$$\omega_{\mathrm{FW}} = \sqrt{\left[\frac{L_s^2 L_r^2 + (L_s L_r - L_m^2)^2}{2L_s^2 (L_s L_r - L_m^2)^2}\right]} \frac{V_{s(max)}}{I_{s(max)}} \tag{25}$$

which will serve to analyze the proposed controller by considering speed values in both regions. At last, Figure 5 shows the d current value versus the current rotor speed ω_m of the SPIM.

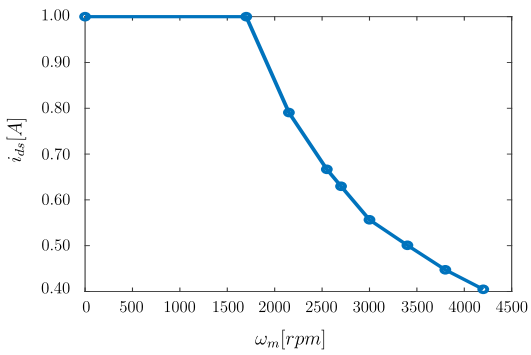

Figure 5. Field current i_{ds} versus rotor speed ω_m graph.

4. Experimental Results

The MPCC technique along the FW algorithm is tested to validate its performance over the experimental bench.

4.1. Experimental Bench Composition

The experimental setup consists of a SPIM driven by two conventional three-leg VSIs, and a dc power supply is used to provide a constant dc-link. The activation of the VSIs is achieved through a real-time rapid prototyping platform named dSPACE MABXII DS1401 in conjunction with MATLAB/Simulink. The SPIM parameters were obtained through stand-still tests and AC time domain conventional methods [35], listed in Table 1. The results that are obtained are then processed using a custom MATLAB script. The current was measured using LA 55-P s sensors, with multiple turns to enhance accuracy at low measurements values and a frequency range from dc to 200 kHz. These measured values are digitized with a 16-bit A/D converter. At the same time, the SPIM mechanical angle and speed are obtained by using a 1024 ppr incremental encoder. Moreover, a 5 HP eddy current brake is applied to the SPIM to perform a variable mechanical load. The experimental setup is illustrated in Figure 6.

Table 1. SPIM physical parameters.

Parameter	Value	Parameter	Value
R_r (Ω)	6.9	R_s (Ω)	6.7
L_s (mH)	654.4	L_r (mH)	626.8
L_m (mH)	614	L_{ls} (mH)	5.3
ω_{m-nom} (r/min)	2540	P_w (kW)	2
J_i (kg.m^2)	0.07	B_i (kg.m^2/s)	0.0004
P	1	$Slip$	0.1533
T_{e-nom} (Nm)	7.5	i_{s-rms} (A)	2.2

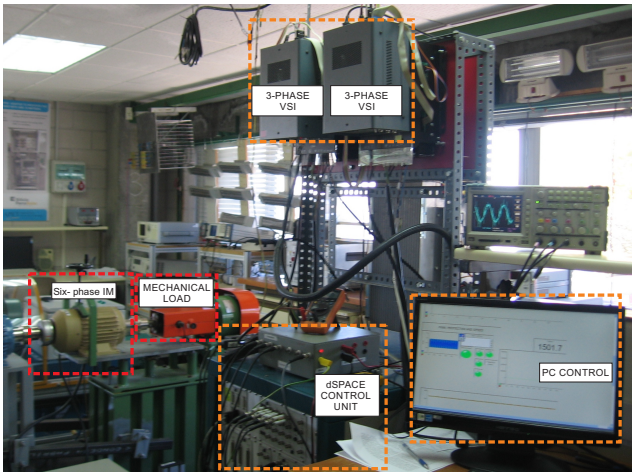

Figure 6. Experimental bench diagram with the SPIM, the VSI, the dSPACE platform, and the eddy current brake.

The cost function in (11) with $\lambda_{xy} = 0.1$ is selected to analyze the controller. It is worth mentioning that λ_{xy} is estimated by a heuristic method and focuses on a sub-optimal result. At last, by using the autocovariance-least square (ALS) technique, the measurement and process noise values can be obtained since it provides an unbiased estimate with the lowest covariance. This method is further explained in [31] and is defined as $\hat{Q}_w = 0.0022$ and $\hat{R}_v = 0.0022$.

4.2. Figures of Merit

The experimental results examine the controller in terms of the MSE of the stator currents in every plane. On the other hand, the THD is obtained in the $(\alpha - \beta)$ plane. The MSE is calculated in the following equation:

$$\text{MSE}(i_{s\Phi}) = \sqrt{\frac{1}{N}\sum_{k=1}^{N}(i_{s\Phi}[k] - i^*_{s\Phi}[k])^2} \tag{26}$$

where N is the total number of tested samples, $i_{s\Phi}$ the measured stator current, $i^*_{s\Phi}$ is the stator current reference, and $\Phi \in \{\alpha, \beta, x, y\}$. Lastly, the THD is obtained as follows:

$$\text{THD}(i_s) = \sqrt{\frac{1}{i^2_{s1}}\sum_{j=2}^{N}(i_{sj})^2} \tag{27}$$

where i_{s1} and i_{sj} are the fundamental and harmonic stator currents, respectively.

4.3. Steady-State Results

For every test, the $(x - y)$ values are zero ($i^*_{xs} = i^*_{ys} = 0$) since this plane is related only to the machine's losses. A defined d value ($i^*_{ds} = 1$ A) is set in rated speed conditions.

The sampling frequency is fixed to 16 kHz. For hardware limitations, i.e., the maximum encoder speed and the eddy current brake, the dc power source is reduced to 65% of the nominal value, fixed to 400 V, and the rated speed is now considered 1700 r/min. Steady-state tests are performed at different mechanical speeds: 1700 r/min (rated), 2150 r/min (+25% rated), 2550 r/min (+50% rated), 3000 r/min (+75% rated), and 3400 r/min (+100% rated).

Tables 2 and 3 present the results for different speeds for the standard MPCC and the one equipped with the field-weakening (named MPCC-FW), respectively, regarding the MSE of the rotor speed and stator currents in the $(\alpha - \beta)$, $(x - y)$, and $(d - q)$ planes and the THD for the $(\alpha - \beta)$ currents. The results show great behavior of MPCC at the rated speed for $(\alpha - \beta)$ and $(d - q)$ tracking, $(x - y)$ reduction, and the rotor speed tracking. It must be considered that the tests at 3800 and 4200 r/min were carried out with a reduced mechanical load to reach these speeds, considering that they already twice exceed the rated speed under these conditions.

At 25% above the rated speed, MPCC has better current tracking in all planes compared to the MPCC-FW technique. This speed is very close to $\omega_{\mathrm{FW}} = 2170$ r/min, showing that, in the first region of FW, MPCC has a good performance, especially in current tracking. At 50% above the rated speed, MPCC-FW is better at current tracking in the $(\alpha - \beta)$ and $(x - y)$ planes than MPCC but is worse in the d current. The THD is also better in MPCC-FW than the MSE for the q current, but for the d current, it is significantly worse. At twice the rated speed, only MPCC-FW can operate, and it shows great results in almost every aspect except for d current tracking.

Table 2. Behavior results of stator currents: MSE (A), MSE (r/min), and THD (%) for MPCC at different mechanical speeds (r/min).

ω_m^*	$\mathbf{MSE}_\alpha$	$\mathbf{MSE}_\beta$	$\mathbf{MSE}_x$	$\mathbf{MSE}_y$	$\mathbf{MSE}_{\omega_m}$
1700	0.0973	0.1076	0.2011	0.2033	4.44
2150	0.1497	0.1593	0.2291	0.2305	3.98
2550	0.1359	0.1461	0.2527	0.2476	3.98
ω_m^*	$\mathbf{THD}_\alpha$	$\mathbf{THD}_\beta$	$\mathbf{MSE}_d$	$\mathbf{MSE}_q$	
1700	10.57	11.95	0.0792	0.1216	
2150	11.88	12.24	0.0793	0.2037	
2550	7.82	8.18	0.0743	0.1852	

Table 3. Behavior results of stator currents: MSE (A), MSE (r/min), and THD (%) for MPCC-FW algorithm at different mechanical speeds (r/min).

ω_m^*	$\mathbf{MSE}_\alpha$	$\mathbf{MSE}_\beta$	$\mathbf{MSE}_x$	$\mathbf{MSE}_y$	$\mathbf{MSE}_{\omega_m}$
2150	0.1618	0.1608	0.2352	0.2311	3.50
2550	0.1237	0.1287	0.2325	0.2373	3.36
3000	0.1912	0.1957	0.2755	0.2700	4.27
3400	0.1773	0.1796	0.2828	0.2763	8.54
3800	0.1702	0.1724	0.1924	0.1929	6.26
4200	0.1642	0.1693	0.1976	0.2019	
ω_m^*	$\mathbf{THD}_\alpha$	$\mathbf{THD}_\beta$	$\mathbf{MSE}_d$	$\mathbf{MSE}_q$	
2150	10.77	11.13	0.0912	0.2091	
2550	7.45	8.10	0.1104	0.1402	
3000	6.48	6.90	0.1593	0.2224	
3400	5.07	5.11	0.1936	0.1619	
3800	22.96	22.73	0.0988	0.2211	
4200	23.44	23.93	0.1029	0.2122	

Figure 7 presents a polar representation of the stator currents in the $(\alpha - \beta)$ and $(x - y)$ planes for MPCC and MPCC-FW under different speed conditions. These tests are performed with a fixed mechanical load. So, the $(\alpha - \beta)$ amplitude varies for different rotor speeds. They depict low $(x - y)$ currents in every condition, especially at 3400 r/min (double-rated speed). At the same time, Figure 8 illustrates the α and x currents, as well as the reference and measured rotor speed for the same speed conditions as Figure 7.

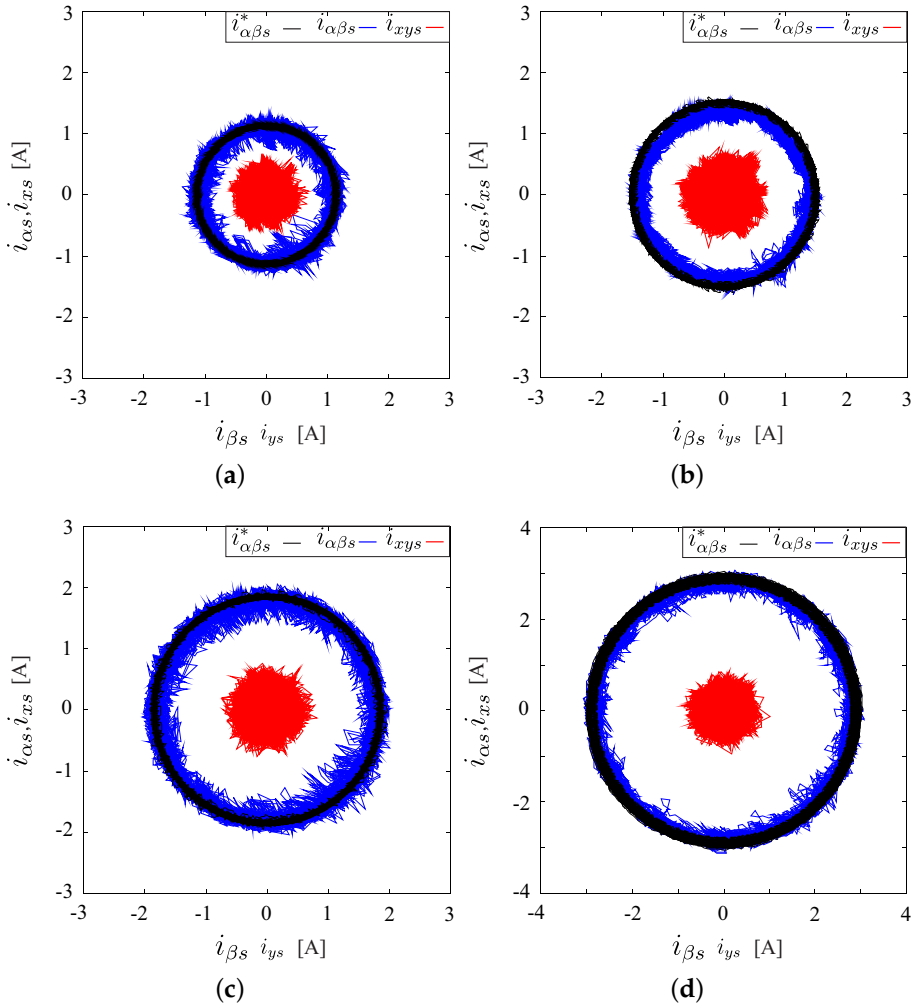

Figure 7. Polar representation of stator currents at different speeds for both MPCC and MPCC-FW: (**a**) MPCC at 1700 r/min; (**b**) MPCC at 2550 r/min; (**c**) MPCC-FW at 2550 r/min; and (**d**) MPCC-FW at 3400 r/min.

The computational burden for PCC, MPCC, and MPCC-FW is worth considering. The amount of floating point operations (FPOs) is considered to generalize the cost in different control boards. PCC is considered to have 49 iterations, and every iteration has 48 FPOs from the prediction equation, including the cost function, giving a total of 2352 FPOs. MPCC is considered to have 12 iterations with 228 FPOs for 2736 FPOs. MPCC-FW only includes the FW algorithm outside MPCC, which only adds four for 2740 FPOs.

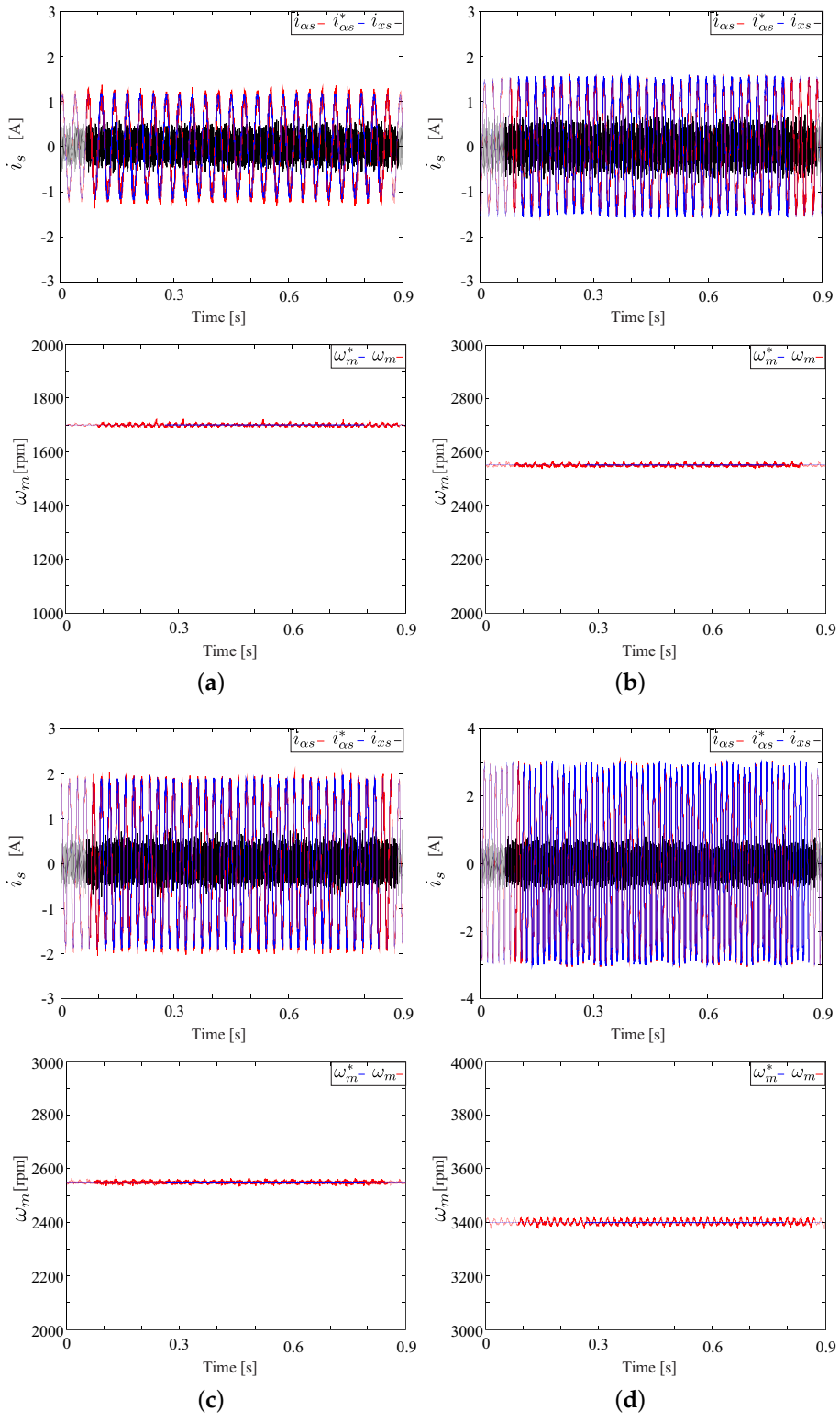

Figure 8. Stator currents $i_{\alpha s}$, $i^*_{\alpha s}$, and i_{xs} at different speeds for both MPCC and MPCC-FW: (**a**) MPCC at 1700 r/min; (**b**) MPCC at 2550 r/min; (**c**) MPCC-FW at 2550 r/min; and (**d**) MPCC-FW at 3400 r/min.

4.4. Transient Results

For this analysis, a change in the mechanical speed is considered from 1700 (nominal) to 2550 r/min (+50% nominal) for both techniques. Figure 9 presents the dynamic behavior (the performance of the $(d-q)$ and $(\alpha-\beta)$ stator currents) for both MPCC and MPCC-FW.

The step change is shown at the instant of 5 ms where MPCC has a reaching time of 6.9 ms and 7.5 ms for the d and q currents, respectively. As for MPCC-FW, the reaching time is 4.75 ms and 9.6 ms for the d and q currents, respectively. In both cases, for only the d current, they present a current drop, which is 55 % and 69 % for MPCC and MPCC-FW, respectively, where the reduction in the magnetic field intensity at that moment of speed change is confirmed due to the entry into the FW zone. However, it is also possible to appreciate the response speed of the controller that manages to stabilize the currents in a short period. It is worth mentioning that the $(d-q)$ plane has a coupling in MPCC. At the same time, it is considered that MPCC-FW has a reduction in the d current reference as the speed increases.

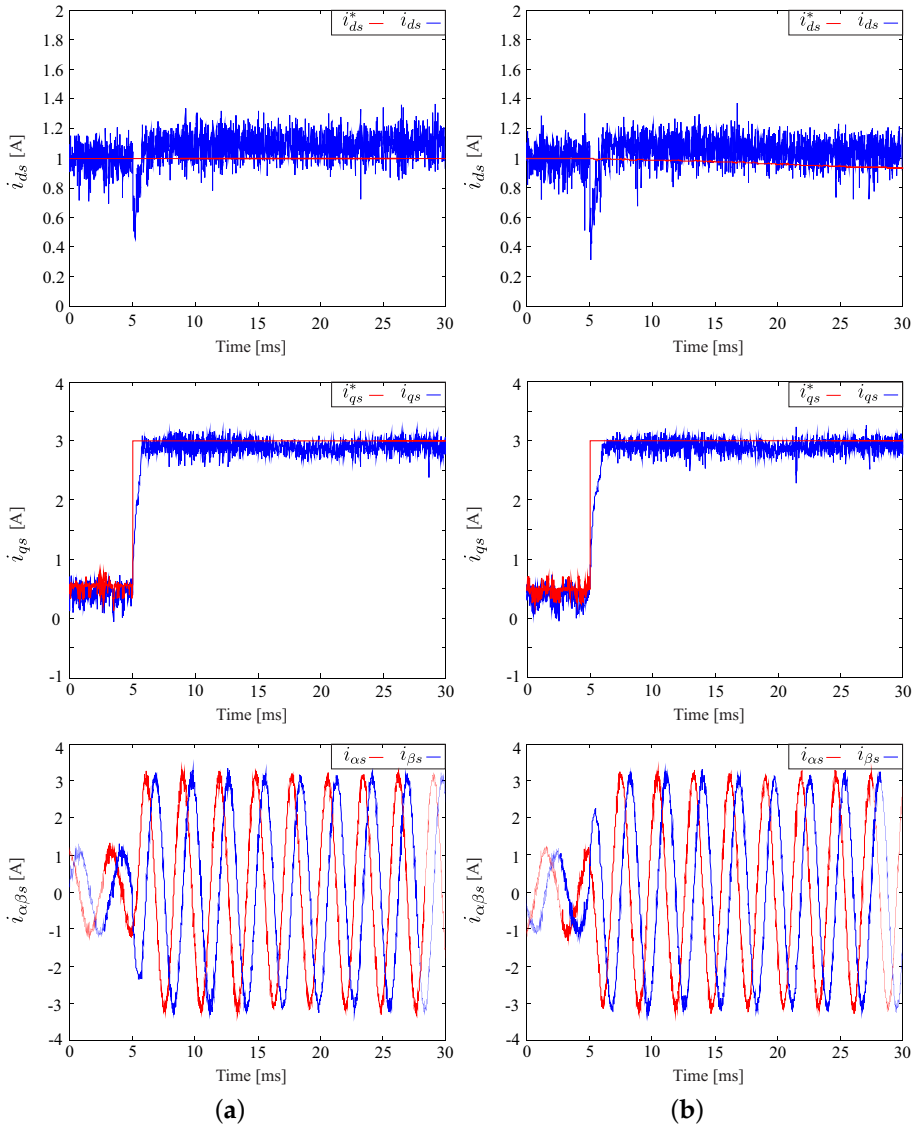

Figure 9. Transient response of stator currents $(d-q)$ and $(\alpha-\beta)$ from a speed step response of 1700 r/min to 2550 r/min (i_{qs} response of 0.5 to 3 A): (**a**) MPCC and (**b**) MPCC-FW.

4.5. Robustness Results

The robustness results consist of the comparison between MPCC and MPCC-FW at a $\pm$25% change from the rated value of L_m, which represents the most sensitive variable in induction machines [36]. Tables 4 and 5 present the behavior with a $\pm$25% change from the rated value for both MPCC and MPCC-FW to test the control robustness.

Table 4. Behavior results of stator currents for MPCC under ±25% of change from the rated L_m.

+25% of Rated L_m					
ω_m^*	MSE_α	MSE_β	MSE_x	MSE_y	MSE_{ω_m}
2550	0.1750	0.1758	0.2592	0.2503	3.93
ω_m^*	THD_α	THD_β	MSE_d	MSE_q	
2550	9.68	9.64	0.0765	0.2360	
−25% of rated L_m					
ω_m^*	MSE_α	MSE_β	MSE_x	MSE_y	MSE_{ω_m}
2550	0.1712	0.1762	0.2578	0.2515	4.09
ω_m^*	THD_α	THD_β	MSE_d	MSE_q	
2550	8.83	9.08	0.0728	0.2347	

Table 5. Behavior results of stator currents for MPCC-FW under ±25% of change from the rated L_m.

+25% of Rated L_m					
ω_m^*	MSE_α	MSE_β	MSE_x	MSE_y	MSE_{ω_m}
2550	0.1804	0.1800	0.2561	0.2541	4.05
ω_m^*	THD_α	THD_β	MSE_d	MSE_q	
2550	8.74	9.04	0.1140	0.2279	
−25% of rated L_m					
ω_m^*	MSE_α	MSE_β	MSE_x	MSE_y	MSE_{ω_m}
2550	0.1622	0.1642	0.2534	0.2472	4.24
ω_m^*	THD_α	THD_β	MSE_d	MSE_q	
2550	8.63	8.96	0.1088	0.2035	

The tests demonstrated that for MPCC, there is no significant difference between the performances of +25 and −25% rated L_m, but they are slightly worse than with the rated value, especially for the q and $(\alpha - \beta)$ current tracking. At the same time, MPCC-FW presents better performance for −25% rated L_m but worse compared to the rated value. It can be mentioned that the $(x - y)$ currents barely show any change, so both controllers maintain the same level of minimization regarding these currents. MPCC-FW is slightly more sensible than MPCC alone, so it should be considered that in these FW operations, the parameters must be precise to obtain optimal performance.

4.6. Comparative Analysis

In this subsection, results from other techniques published in the literature are compared. Table 6 presents the results for a modulated predictive controller defined as M2PC [37] with FW, and Table 7 for another MPCC with virtual vectors, named MPCC-VV-FSF [38] with FW.

It can be observed that MPCC-FW presents better performance for the figures of merit compared to the two techniques already published, except in the $(x - y)$ regulation, in which M2PC-VV reduces up to 80%. Particularly, it is shown that MPCC has better results at higher speeds, including speed tracking, in which the other two techniques present an appreciable steady-state error.

Finally, it should be noted that the classic MPC does not achieve stable behavior at higher speeds, as published in [24], so comparison results with it were not included.

Table 6. Performance behavior of stator currents: MSE (A), MSE (r/min), and THD (%) for M2PC [37] with FW algorithm at different mechanical speeds (r/min).

ω_m^*	$\mathbf{MSE}_\alpha$	$\mathbf{MSE}_\beta$	$\mathbf{MSE}_x$	$\mathbf{MSE}_y$	$\mathbf{MSE}_{\omega_m}$
2150	0.1765	0.1837	0.1668	0.1689	2.5662
2550	0.2400	0.2447	0.1885	0.1932	2.4694
3000	0.3552	0.3574	0.2207	0.2296	3.6711
3400	0.4119	0.4102	0.2331	0.2430	227.28
ω_m^*	$\mathbf{THD}_\alpha$	$\mathbf{THD}_\beta$	$\mathbf{MSE}_d$	$\mathbf{MSE}_q$	
2150	11.07	12.67	0.1503	0.2057	
2550	10.34	11.06	0.2285	0.2555	
3000	9.82	9.83	0.3693	0.3429	
3400	9.13	9.43	0.4415	0.3781	

Table 7. Performance behavior of stator currents: MSE (A), MSE (r/min), and THD (%) for MPCC-VV-FSF [38] with FW algorithm at different mechanical speeds (r/min).

ω_m^*	$\mathbf{MSE}_\alpha$	$\mathbf{MSE}_\beta$	$\mathbf{MSE}_x$	$\mathbf{MSE}_y$	$\mathbf{MSE}_{\omega_m}$
2150	0.1692	0.1762	0.1251	0.1267	2.2272
2550	0.2580	0.2633	0.1397	0.1429	2.1261
3000	0.3859	0.3883	0.1591	0.1651	3.0635
3400	0.4529	0.4505	0.1634	0.1702	223.54
ω_m^*	$\mathbf{THD}_\alpha$	$\mathbf{THD}_\beta$	$\mathbf{MSE}_d$	$\mathbf{MSE}_q$	
2150	10.46	11.15	0.1616	0.2214	
2550	11.02	12.13	0.2485	0.2776	
3000	10.92	11.03	0.4059	0.3765	
3400	10.22	10.45	0.4908	0.4198	

5. Conclusions

This paper presented a study and implementation of a modulated PCC, named MPCC, with an FW algorithm to extend its range of operation for a SPIM. The experimental tests demonstrated their effectiveness and were compared with MPCC without the FW algorithm. The tests were performed under different steady and transient conditions. The results showed that MPCC alone is a refined technique in conditions above the rated speed due to its better use of the dc-link by synthesizing its active vectors. Notably, the performance is better than with the FW algorithm at speeds below ω_{FW}, which defines two regions: one above the rated speed and one approximately 1.25 times the rated speed. For speeds above this value, MPCC-FW performed very well, surpassing double the rated speed, highlighting the $(x-y)$ currents reduction and the low THD for the $(\alpha-\beta)$ currents. Compared to other modulation techniques, MPCC-FW presents better stator current tracking for $(\alpha-\beta)$ and $(d-q)$, especially when operating at higher speeds reaching improvement values of 50%. As a limitation of this proposed method, it was not yet possible to correct the steady-state error in the $(d-q)$ currents, which is accentuated in the FW zone. This is why it is a topic for future work. Therefore, the proposed technique is valid for conditions above the rated speed, which is a standard condition in industrial applications.

Author Contributions: Conceptualization, M.A.; methodology, M.A. and J.D.-G.; software, M.A., J.D.-G. and O.G.; validation, J.D.-G. and M.A.; formal analysis, M.A., O.G., L.D. and C.R.; investigation, M.A., O.G., L.D., C.R. and A.F.; resources, J.D.-G. and M.A.; data curation, M.A. and O.G.; writing—original draft preparation, M.A., J.R., O.G., L.D., C.R. and R.G.; writing—review and editing, M.A., J.R., O.G., L.D., C.R. R.G. and A.F.; visualization, M.A. and J.D.-G.; supervision, M.A.; project administration, M.A. and O.G.; funding acquisition, M.A. All authors have read and agreed to the published version of the manuscript.

Funding: M. Ayala acknowledges the support of Conacyt through INIC01-35. J. Doval-Gandoy acknowledges the Government of Galicia under Grant GPC-ED431B 2023/12 and in part by the Spanish State Research Agency (AEI) under Project PID2022-136908OB-I00/MCIN/AEI/10.13039/501100011033/FEDER-UE

Institutional Review Board Statement: Not applicable.

Informed Consent Statement: Not applicable.

Data Availability Statement: The original contributions presented in the study are included in the article, further inquiries can be directed to the corresponding authors.

Acknowledgments: M. Ayala, J. Rodas, O. Gonzalez, R. Gregor, L. Delorme, and C. Romero also acknowledge the support of the Consejo Nacional de Ciencia y Tecnología (CONACYT)-Paraguay through its PRONII program.

Conflicts of Interest: The authors declare no conflict of interest.

Abbreviations

These abbreviations are described in this work:

FCS-MPC	Finite control version of model predictive control
FOC	Field-oriented control
FW	Field weakening
IGBT	Isolated gate bipolar transistor
IRFOC	Indirect rotor field-oriented control
KF	Kalman filter
LO	Luenberger observer
LV	Large vector
MV	Mid vector
MPCC	Modulated predictive control
MSE	Mean square error
PCC	Predictive current control
PI	Proportional-integral
SPIM	Six-phase induction machine
SVM	Space vector modulation
THD	Total harmonic distortion
VSD	Vector space decomposition
VSI	Voltage source inverter
ZV	Null vector

References

1. Levi, E. Advances in Converter Control and Innovative Exploitation of Additional Degrees of Freedom for Multiphase Machines. *IEEE Trans. Ind. Electron.* **2016**, *63*, 433–448. [CrossRef]
2. Barrero, F.; Duran, M.J. Recent Advances in the Design, Modeling, and Control of Multiphase Machines: Part I. *IEEE Trans. Ind. Electron.* **2016**, *63*, 449–458. [CrossRef]
3. Liu, Z.; Li, Y.; Zheng, Z. A review of drive techniques for multiphase machines. *CES Trans. Electr. Mach. Syst.* **2018**, *2*, 243–251. [CrossRef]
4. Duran, M.J.; Barrero, F. Recent Advances in the Design, Modeling, and Control of Multiphase Machines: Part II. *IEEE Trans. Ind. Electron.* **2016**, *63*, 459–468. [CrossRef]
5. Peng, X.; Liu, Z.; Jiang, D. A review of multiphase energy conversion in wind power generation. *Renew. Sustain. Energy Rev.* **2021**, *147*, 111172. [CrossRef]
6. Prieto, I.G.; Duran, M.J.; Garcia-Entrambasaguas, P.; Bermudez, M. Field-oriented control of multiphase drives with passive fault tolerance. *IEEE Trans. Ind. Electron.* **2019**, *67*, 7228–7238. [CrossRef]
7. Heidari, H.; Rassõlkin, A.; Vaimann, T.; Kallaste, A.; Taheri, A.; Holakooie, M.H.; Belahcen, A. A novel vector control strategy for a six-phase induction motor with low torque ripples and harmonic currents. *Energies* **2019**, *12*, 1102. [CrossRef]
8. Holakooie, M.H.; Iwanski, G.; Miazga, T. Switching-Table-Based Direct Torque Control of Six-Phase Drives With *xy* Current Regulation. *IEEE Trans. Ind. Electron.* **2022**, *69*, 11890–11902.

[CrossRef]
9. Zaidi, E.; Marouani, K.; Bouadi, H.; Nounou, K.; Aissani, M.; Bentouhami, L. Control of a multiphase machine fed by multilevel inverter based on sliding mode controller. In Proceedings of the 2019 IEEE International Conference on Environment and Electrical Engineering and 2019 IEEE Industrial and Commercial Power Systems Europe (EEEIC/I&CPS Europe), Genova, Italy, 11–14 June 2019; pp. 1–6. [CrossRef]
10. Mossa, M.A.; Echeikh, H.; El Ouanjli, N.; Alhelou, H.H. Enhanced Second-Order Sliding Mode Control Technique for a Five-Phase Induction Motor. *Int. Transact. Electr. Energy Syst.* **2022**, *2022*, 8215525. [CrossRef]
11. Rodriguez, J.; Garcia, C.; Mora, A.; Flores-Bahamonde, F.; Acuna, P.; Novak, M.; Zhang, Y.; Tarisciotti, L.; Davari, S.A.; Zhang, Z.; et al. Latest advances of model predictive control in electrical drives—Part I: Basic concepts and advanced strategies. *IEEE Trans. Power Electron.* **2021**, *37*, 3927–3942. [CrossRef]
12. Duran, M.J.; Gonzalez-Prieto, I.; Gonzalez-Prieto, A.; Aciego, J.J. The Evolution of Model Predictive Control in Multiphase Electric Drives: A Growing Field of Research. *IEEE Ind. Electron. Mag.* **2022**, *16*, 29–39. [CrossRef]
13. Gonzalez-Prieto, I.; Duran, M.J.; Aciego, J.J.; Martin, C.; Barrero, F. Model predictive control of six-phase induction motor drives using virtual voltage vectors. *IEEE Trans. Ind. Electron.* **2017**, *65*, 27–37. [CrossRef]
14. Aciego, J.J.; Prieto, I.G.; Duran, M.J. Model predictive control of six-phase induction motor drives using two virtual voltage vectors. *IEEE J. Emerg. Sel. Top. Power Electron.* **2018**, *7*, 321–330. [CrossRef]
15. González-Prieto, I.; Durán, M.; Bermúdez, M.; Barrero, F.; Martín, C. Assessment of Virtual-Voltage-based Model Predictive Controllers in Six-phase Drives under Open-Phase Faults. *IEEE J. Emerg. Sel. Top. Power Electron.* **2019**, *8*, 2634–2644. [CrossRef]
16. Ayala, M.; Doval-Gandoy, J.; Rodas, J.; Gonzalez, O.; Gregor, R.; Rivera, M. A novel modulated model predictive control applied to six-phase induction motor drives. *IEEE Trans. Ind. Electron.* **2020**, *68*, 3672–3682. [CrossRef]
17. Sharma, S.; Aware, M.V.; Bhowate, A. Symmetrical six-phase induction motor-based integrated driveline of electric vehicle with predictive control. *IEEE Trans. Transp. Electrif.* **2020**, *6*, 635–646. [CrossRef]
18. Arahal, M.R.; Barrero, F.; Satué, M.G.; Ramírez, D.R. Predictive Control of Multi-Phase Motor for Constant Torque Applications. *Machines* **2022**, *10*, 211. [CrossRef]
19. Zarri, L.; Mengoni, M.; Tani, A.; Serra, G.; Casadei, D.; Ojo, J. Control schemes for field weakening of induction machines: A review. In Proceedings of the 2015 IEEE Workshop on Electrical Machines Design, Control and Diagnosis (WEMDCD), Turin, Italy, 26–27 March 2015; pp. 146–155. [CrossRef]
20. Kim, S.H.; Sul, S.K. Maximum torque control of an induction machine in the field weakening region. *IEEE Trans. Ind. Appl.* **1995**, *31*, 787–794. [CrossRef]
21. Su, J.; Gao, R.; Husain, I. Model predictive control based field-weakening strategy for traction - EV used induction motor. *IEEE Trans. Ind. Appl.* **2017**, *54*, 2295–2305. [CrossRef]
22. Zhang, Y.; Zhang, B.; Yang, H.; Norambuena, M.; Rodriguez, J. Generalized sequential model predictive control of IM drives with field-weakening ability. *IEEE Trans. Power Electron.* **2018**, *34*, 8944–8955. [CrossRef]
23. Xu, W.; Tang, Y.; Dong, D.; Xiao, X.; Rashad, E.E.M.; Junejo, A.K. Optimal reference primary flux based model predictive control of linear induction machine with MTPA and field-weakening operations for urban transit. *IEEE Trans. Ind. Appl.* **2022**, *58*, 4708–4721. [CrossRef]
24. Ayala, M.; Doval-Gandoy, J.; Gonzalez, O.; Rodas, J.; Gregor, R.; Rivera, M. Experimental stability study of modulated model predictive current controllers applied to six-phase induction motor drives. *IEEE Trans. Power Electron.* **2021**, *36*, 13275–13284. [CrossRef]
25. Xu, X.; Novotny, D.W. Selection of the flux reference for induction machine drives in the field weakening region. *IEEE Trans. Ind. Appl.* **1992**, *28*, 1353–1358. [CrossRef]
26. Zhao, Y.; Lipo, T. Space vector PWM control of dual three-phase induction machine using vector space decomposition. *IEEE Trans. Ind. Electron.* **1995**, *31*, 1100–1109. [CrossRef]
27. Harnefors, L.; Saarakkala, S.E.; Hinkkanen, M. Speed control of electrical drives using classical control methods. *IEEE Trans. Ind. Appl.* **2013**, *49*, 889–898. [CrossRef]
28. Martin, C.; Arahal, M.; Barrero, F.; Duran, M. Five-Phase Induction Motor Rotor Current Observer for Finite Control Set Model Predictive Control of Stator Current. *IEEE Trans. Ind. Electron.* **2016**, *63*, 4527–4538. [CrossRef]
29. Wang, B.; Luo, C.; Yu, Y.; Wang, G.; Xu, D. Antidisturbance speed control for induction machine drives using high-order fast terminal sliding-mode load torque observer. *IEEE Trans. Power Electron.* **2017**, *33*, 7927–7937. [CrossRef]
30. Yang, Z.; Zhang, D.; Sun, X.; Ye, X. Adaptive exponential sliding mode control for a bearingless induction motor based on a disturbance observer. *IEEE Access* **2018**, *6*, 35425–35434. [CrossRef]
31. Rodas, J.; Barrero, F.; Arahal, M.R.; Martín, C.; Gregor, R. Online estimation of rotor variables in predictive current controllers: A case study using five-phase induction machines. *IEEE Trans. Ind. Electron.* **2016**, *63*, 5348–5356. [CrossRef]
32. Novak, M.; Dragicevic, T.; Blaabjerg, F. Weighting factor design based on Artificial Neural Network for Finite Set MPC operated 3L-NPC converter. In Proceedings of the 2019 IEEE Applied Power Electronics Conference and Exposition (APEC), Anaheim, CA, USA, 17–21 March 2019; pp. 77–82. [CrossRef]
33. Majmunović, B.; Dragičević, T.; Blaabjerg, F. Multi Objective Modulated Model Predictive Control of Stand-Alone Voltage Source Converters. *IEEE J. Emerg. Sel. Top. Power Electron.* **2019**, *8*, 2559–2571. [CrossRef]

34. Van Der Broeck, H.W.; Skudelny, H.C.; Stanke, G.V. Analysis and realization of a pulsewidth modulator based on voltage space vectors. *IEEE Trans. Ind. Appl.* **1988**, *24*, 142–150. [CrossRef]
35. Riveros, J.A.; Yepes, A.G.; Barrero, F.; Doval-Gandoy, J.; Bogado, B.; Lopez, O.; Jones, M.; Levi, E. Parameter identification of multiphase induction machines with distributed windings —Part II: Time-domain techniques. *IEEE Trans. Energy Conv.* **2012**, *27*, 1067–1077. [CrossRef]
36. Wang, F.; Zhang, Z.; Mei, X.; Rodríguez, J.; Kennel, R. Advanced control strategies of induction machine: Field oriented control, direct torque control and model predictive control. *Energies* **2018**, *11*, 120. [CrossRef]
37. Gonzalez, O.; Ayala, M.; Doval-Gandoy, J.; Rodas, J.; Gregor, R.; Rivera, M. Predictive-Fixed Switching Current Control Strategy Applied to Six-Phase Induction Machine. *Energies* **2019**, *12*, 2294. [CrossRef]
38. Gonzalez, O.; Ayala, M.; Romero, C.; Delorme, L.; Rodas, J.; Gregor, R.; Gonzalez-Prieto, I.; Durán, M.J. Model predictive current control of six-phase induction motor drives using virtual vectors and space vector modulation. *IEEE Trans. Power Electron.* **2022**, *37*, 7617–7628. [CrossRef]